# Designing multifunctionality via assembling dissimilar materials: the case of epitaxial AlN/ScN superlattices

Zhijun Jiang,[1,2,3,4] Charles Paillard,[3] David Vanderbilt,[5] Hongjun Xiang,[1,2,*] and L. Bellaiche[3,†]

[1]*Key Laboratory of Computational Physical Sciences (Ministry of Education), State Key Laboratory of Surface Physics, and Department of Physics, Fudan University, Shanghai 200433, China*

[2]*Collaborative Innovation Center of Advanced Microstructures, Nanjing 210093, China*

[3]*Physics Department and Institute for Nanoscience and Engineering, University of Arkansas, Fayetteville, Arkansas 72701, USA*

[4]*School of Physics and Optoelectronic Engineering, Ludong University, Yantai 264025, China*

[5]*Department of Physics and Astronomy, Rutgers University, Piscataway, New Jersey 08854, USA*

## Abstract

First-principles calculations are performed to investigate the effect of epitaxial strain on energetic, structural, electrical, electronic and optical properties of $1 \times 1$ AlN/ScN superlattice. This system is predicted to adopt four different strain regions exhibiting different properties, including optimization of various physical responses such as piezoelectricity, electro-optic coefficient, elasto-optic conversion and elasticity. Varying the strain between these four different regions also allows to create an electrical polarization in a nominally paraelectric material, as a result of a softening of the lowest optical mode, and even to control its magnitude up to a giant value. Furthermore, it results in an electronic band gap that can not only change its nature (direct versus indirect), but also cover a wide range of the electromagnetic spectra from the cyan color to middle ultraviolet (via blue, violet and near ultraviolet). The present findings therefore point out the potential of assembling two different materials inside the same heterostructure to design multifunctionality and striking phenomena.

For technological purposes, having multifunctional materials for which several properties can be simultaneously controlled or optimized at the same time is highly desired [1]. One possible idea for designing such multifunctional materials is to bring together within the same heterostructure two compounds that have separately different structural phases, and play with an external control knob to go from one of these phases to another via transitions. One example to test this idea is to (i) combine AlN (or GaN or InN) with ScN to form superlattices, since AlN, GaN and InN ground states are wurtzite [2, 3] while ScN has been predicted to exhibit a (meta)stable layered phase in its hexagonal form [4–6]; and (ii) choosing the control knob to be the epitaxial strain, since it is known to be an effective tool to enhance physical properties and generate novel phenomena [7–13]. For instance, epitaxial strain can render the nominally paraelectric $SrTiO_3$ to become ferroelectric [8, 9], as well as induce phase transitions, large piezoelectric, dielectric, elasto-optic and electro-optic responses in many systems (see, e.g., Refs. [7, 11–13]).

Moreover, GaN/ScN and InN/ScN superlattices have been predicted to experience under hydrostatic pressure a rare phenomenon [14], namely the existence of so-called *isostructural* phase transitions (see, e.g., Refs. [15–17] and references therein). This further emphasizes the potential for ScN-based superlattices to have striking fundamental features but also for dramatic change and/or optimization of various physical properties as a result of phase transitions [18]. Some (Ga,Sc)N and (In,Sc)N ordered alloys have also been predicted to exhibit symmetry-breaking transitions between different phases when under epitaxial strain, accompanied by a large piezoelectricity [19]. On the other hand, we are not aware of any theoretical or experimental investigation of AlN/ScN superlattices, despite the fact that a large piezoelectric coefficient $d_{33}$ and ferroelectric switching have both been observed in *disordered* $Sc_xAl_{1-x}N$ alloys [20, 21] as a result of the transformation towards a polar structure of the aforementioned predicted peculiar layered phase of pure ScN.

The aim of this Letter is to investigate the effect of epitaxial strain on the properties of AlN/ScN superlattices. As we will see, many different physical properties (e.g., structural, electrical, electronic, optical, elasto-optic and electro-optic behaviors) can be altered and optimized, partly because of the strain-driven occurrence of a phase transition.

This work focuses on properties of epitaxial $1 \times 1$ AlN/ScN superlattice as a function of its in-plane lattice constant (note that results for epitaxial $1 \times 3$ AlN/ScN superlattices are also provided in the Supplemental Material [22]). In the following, $\eta_{in} = (a - a_{eq})/a_{eq}$ characterizes the magnitude of the epitaxial strain, with the zero of strain corresponding to the in-plane lattice constant, $a_{eq}$, of the equilibrium structure (i.e., the one yielding the lowest total energy). We also

limited the calculations for strains ranging between $-6\%$ and $+6\%$.

Here, we perform first-principle calculations (computational details are given in the Supplemental Material [22]) to predict (i) structural parameters, with our present results being estimated to underestimate the lattice parameters of $1 \times 1$ AlN/ScN by about $0.78\%$; (ii) electronic band gaps, with our computational data being estimated to underestimate the experimental values by about $1.4$ eV in the studied $1 \times 1$ AlN/ScN superlattice; (iii) electrical polarization; (iv) the $S_{33}^{\rm epi}$ elastic compliance element; (v) $e_{33}$ piezoelectric stress coefficients; (vi) $d_{33}^{\rm epi}$ piezoelectric strain coefficients; and (vii) elasto-optic coefficients, $p_{ij}$ (in Voigt notation).

Furthermore, we also predicted electro-optic (EO) coefficients via the density functional perturbation theory, which is based on the linear response of the optical dielectric tensor induced by a static (or low frequency) electric field $\mathcal{E}_k$ [25, 26]. Practically, the linear EO (Pockels) effect is described by the third-rank EO tensor $r_{ijk}$:

$$\Delta(\varepsilon^{-1})_{ij} = \sum_{k=1}^{3} r_{ijk}\mathcal{E}_k, \tag{1}$$

where $(\varepsilon^{-1})_{ij}$ is the inverse of the optical dielectric tensor (approximated by the electronic dielectric tensor). As emphasized in Refs. [13, 25, 26], two different types of EO coefficients should be distinguished, that are the clamped (strain-free) *versus* the unclamped (namely, stress-free for $\sigma_{33}$ but clamped in-plane stresses) ones. The clamped EO tensor, $r_{ijk}^{\eta}$, can be expressed as a sum of two contributions: (1) a bare electronic part, $r_{ijk}^{\rm el}$, which depends on the nonlinear optical dielectric susceptibility $\chi_{ijk}^{(2)}$ (which defines the second-order change of the induced-polarization with respect to $\mathcal{E}_k$); and (2) an ionic contribution, $r_{ijk}^{\rm ion}$, which depends on the first-order change of the linear dielectric susceptibility due to atomic displacements. This ionic contribution is related to the Raman susceptibility $\alpha_{ij}^{\rm m}$ of mode $\rm m$ and polarity $p_k^{\rm m}$ of a transverse optical mode of frequency $\omega_m$(directly linked to the infrared intensities). One thus has:

$$r_{ijk}^{\eta} = r_{ijk}^{\rm el} + r_{ijk}^{\rm ion} = \frac{-8\pi}{n_i^2 n_j^2}\chi_{ijk}^{(2)} - \frac{4\pi}{n_i^2 n_j^2 \sqrt{\Omega_0}} \sum_m \frac{\alpha_{ij}^{\rm m} p_k^{\rm m}}{\omega_m^2}, \tag{2}$$

where $n_i$ and $n_j$ are the principal refractive indices, and $\Omega_0$ is the cell volume.

Regarding the unclamped EO coefficients (which are, in many cases, more relevant to technological applications), $r_{ijk}^{\sigma}$, they can be expressed as:

$$r^{\sigma}_{ijk} = r^{\eta}_{ijk} + \sum_{\alpha,\beta} p_{ij\alpha\beta} d^{\rm epi}_{\alpha\beta k}, \tag{3}$$

where $p_{ij\alpha\beta}$ are elasto-optic constants and $d^{\rm epi}_{\alpha\beta k}$ are piezoelectric strain coefficients. In other words, unclamped EO coefficients consist of the sum of the EO clamped coefficients and of a second term involving the products between elasto-optic constants and the piezoelectric strain coefficients.

Let us now present some of our results for various properties of the $1 \times 1$ AlN/ScN superlattice, as a function of the strain in this system. Figure 1(a) reports the resulting total energy, with the zero of energy corresponding to the ground state. Figures 1(b)–1(c) display structural characteristics, in the forms of the $c/a$ axial ratio and internal parameters ($u_{\rm AlN}$ and $u_{\rm ScN}$), respectively (see the Supplemental Material [22] for the definition of these internal parameters). Figure 1(d) shows an electrical quantity via the polarization $P_z$ – which can only be oriented along the out-of-plane axis. Figure 1(e) reports predictions about the vibrational property consisting of phonon frequencies at the $\Gamma$ point. Finally, Fig. 1(f) shows various electronic band gaps, such as the difference in energy between the conduction band minimum and valence band maximum (that we will refer to as the electronic band gap) but also direct band gaps at the $\Gamma$, H and K points of the first Brillouin zone.

Figure 1(a) reveals that $1 \times 1$ AlN/ScN exhibits two minima in the total energy-*versus*-strain curve, that occur at $0\%$ and $-5\%$ strains. They respectively correspond to an hexagonal-derived structure [to be denoted as $h$-derived, and shown in Fig. 2(a)] and a wurtzite-derived phase [to be coined $w$-derived, and displayed in Fig. 2(d)].

Moreover, the strain-induced behaviors of the properties reported in Figs. 1(b)–1(f) allow the determination of four different strain regions. First of all, a Region I pertains to strain ranging between $+6\%$ and $\sim -0.7\%$ and is characterized by an axial ratio and internal parameters (that are strain-independent) being all relatively close to those of the layered hexagonal $h$ phase of ScN (that are $1.21$ and $0.5$, respectively), while $P_z$ are null – as consistent with the paraelectric nature of this $h$-phase in the parent compounds. We can thus classify Region I as $h$-derived. The phase in Region I is numerically found to have the (paraelectric) $P\bar{6}m2$ space group (note that the $h$-phase in pure ScN has a $P6_3/mmc$ space group) [33]. In Region I, the LDA-calculated direct band gap at $\Gamma$ [see blue square in Fig. 1(f)] varies from $1.0$ to $1.92$ eV. Note that correcting the LDA underestimation as indicated above should then lead to a variation from about $2.4$ to $3.32$ eV, which will then correspond to colors covering cyan, blue, violet and ultraviolet, which is promising for some applications (e.g. blue-violet laser and ultraviolet sensor devices) [34–37]. The nature of

the electronic band gap [see red circle in Fig. 1(f)] changes from direct at $\Gamma$, for strains between $+6\%$ and $+1.5\%$, to indirect ($\Gamma$-to-K) between $+1\%$ and $-0.7\%$. Figure 1(e) also reveals that the lowest $A_1^{(1)}$ phonon at the $\Gamma$ point continuously softens towards a zero frequency when decreasing the strain in Region I.

Such softening leads to the appearance of a polar Region II of $P3m1$ symmetry, at which an electrical polarization appears and that extends for $\eta_{in}$ between $\sim -0.7\%$ and $-1.8\%$. In Region II, $c/a$ has a different slope with respect to Region I while the internal parameters now decrease when the compressive strain strengthens in magnitude. Such Region II is associated with an intermediate structure (that is rather close to the $h$-derived structures), for which an example is shown in Fig. 2(b). In this Region II, the LDA electronic band gap is indirect ($\Gamma$-to-K) and varies from $1.67$ to $2.24$ eV (the corrected-with-respect-to-LDA value therefore varies from $3.07$ to $3.64$ eV, which lie in the violet and near ultraviolet regions of the electromagnetic spectrum). In Region II, the direct band gap at the K point linearly and significantly increases when increasing the magnitude of the compressive strain.

The left border of Region II located at $\sim -1.8\%$ and therefore the passage to another Region, to be called Region III (that also has a $P3m1$ space group), is marked by several features. For instance, the direct band gap at the K point stops being sensitive to strain and an *anticrossing* between the two lowest phonon modes of $A_1$ symmetry, that are denoted as $A_1^{(1)}$ and $A_1^{(2)}$ in Fig. 1(e), occurs there. Details of such anticrossing are further provided in the Supplemental Material [22]. The axial ratio in Region III also adopts a linear behavior with strain that is slightly different from that of Region II, until $c/a$ deviates from linearity at about $-3\%$. Such deviation from linearity marks the left border of Region III and the beginning of another region, to be called Region IV. Note that the existence of two slightly different straight lines in Region II versus Region III for the axial ratio is also accompanied by two weakly different straight lines for $u_{\mathrm{ScN}}$ in these two regions – while the polarization significantly increases from $0$ to about $0.48$ C/m$^2$, and then to $0.76$ C/m$^2$ when increasing the magnitude of the compressive strain in Regions II and III, respectively. The structure associated with Region III in the range of about $-1.8\%$ to $-3\%$ is another intermediate phase that is polar but now close to the wurtzite-derived structures [see an example of such structure in Fig. 2(c)]. In terms of electronic structure, the band gap becomes direct again at $\Gamma$ in Region III and varies from $2.24$ to $2.7$ eV according to LDA (the corrected value thus varies from $3.64$ to $4.1$ eV which is associated with the electromagnetic spectrum of near ultraviolet).

Finally, Region IV occurs for compressive strains smaller than $-3\%$ and corresponds to wurtzite-derived structures (which are polar), as evidenced by a $c/a$ axial ratio being close to $1.6$ for large compressive $\eta_{in}$. Like Regions II and III, Region IV adopts the $P3m1$ space group. The right border of Region IV is marked by a direct band gap at the H-point possessing a kink, and is mostly characterized by different behaviors of direct band gaps when enhancing the magnitude of the compressive strain above $3\%$: the one at $\Gamma$ increases while the one at H decreases and the one at the K-point is nearly insensitive to $\eta_{in}$. Due to all these different evolutions, the electronic band gap is direct at the $\Gamma$ point from $\sim -3\%$ to $-4.5\%$ and then direct again but at the H point from $\sim -5\%$ to $-6\%$, with corrected values ranging between $4.1$ to $4.62$ eV (which is associated with the electromagnetic spectrum from near ultraviolet to middle ultraviolet) and then from $4.7$ to $4.6$ eV (which corresponds to middle ultraviolet). Note that ultraviolet sensor devices are important for space communications, bio-medical instrumentation and high temperature plasma research, etc. [38].

It is remarkable that Figs. 1-2 reveal so many striking features: (1) the continuous evolution of the structure from a $h$-derived to a $w$-derived phase; (2) an out-of-plane polarization increasing from 0 to $1.07$ C/m$^2$, when passing through Region II to Region IV, via Region III, with this value of $1.07$ C/m$^2$ being even bigger than the polarization of the tetragonal phase of $PbTiO_3$ films ($0.87$ C/m$^2$) [11]; and (3) the control of the nature (direct *versus* indirect) and value of the electronic band gap, covering the cyan, blue, violet, and near and middle ultraviolet parts of the electromagnetic spectra.

It is also important to know that our theoretical in-plane lattice constant corresponding to $\eta_{in} = 0\%$ is $3.507$ Å in the $1\times1$ AlN/ScN superlattice, which, according to the aforementioned expected underestimation of $0.78\%$ of our predicted lattice parameters, should in fact correspond to a value of $3.534$ Å. As a result, the following substrates should correspond to the following strains: Sc ($3.309$ Å, that is $-6.4\%$), ZnO ($3.2496$ Å, that is $-8\%$), Hf ($3.18$ Å, that is $-10\%$), and wurtzite InN ($3.544$ Å, that is $0.3\%$) [2, 39]. As a result, similar to the strategy demonstrated in Ref. [40], one can envision growing $1\times1$ AlN/ScN superlattices with different thicknesses on such substrates to allow the strain to partially relax by different amounts, which will then result in covering all the strain ranges associated with Regions I, II, III and IV. Note also that the $w$-derived structure of $1\times1$ AlN/ScN can be seen as a (meta)stable polymorph of the $h$-derived ground state of this system, implying that a compressive strain as large as $-6\%$ (with respect to $h$-derived ground state) should be practically reached in our superlattice – consistent with the fact that strain of this

order of magnitude has been experimentally found in $BiFeO_3$ films because of the existence of a metastable T-phase in addition to the R-ground state [41–43].

Let us now reveal the impact of these different regions on physical responses, such as EO and elasto-optic coefficients, piezoelectricity and elastic responses (as reported in Fig. 3). For that, let us first recall that the EO tensor in the $P\bar{6}m2$ space group has one independent nonzero coefficient $r_{22}$, while it has four independent elements in Voigt notations in the $P3m1$ ($C_{3v}$) symmetry: $r_{13}$, $r_{22}$, $r_{33}$ and $r_{42}$. Figures 3(a) and 3(b) display the clamped and unclamped EO coefficients, respectively, as a function of the misfit strain. For the clamped EO coefficients, we indeed obtain $r^{\eta}_{13} = r^{\eta}_{33} = r^{\eta}_{42} = 0$ and very small values of $r^{\eta}_{22}$ in Region I. At the boundary between Regions I and II (i.e., around a compressive strain of $-0.7\%$), a large value of the clamped EO coefficient $r^{\eta}_{33} \simeq 50$ pm/V is predicted, as a result of the aforementioned softening of the $A^{(1)}_1$ mode (see the second term of Eq. (2) indicating that small frequencies should give rise to large clamped coefficients). Strikingly, such a value is larger than the experimental value of $r^{\eta}_{33} \simeq 30.8$ pm/V determined in $LiNbO_3$, which is presently the material of choice for EO applications [44, 45], and than the clamped $r^{\eta}_{33} \simeq 30.5$ pm/V recently predicted in $PbTiO_3$ films by strain-inducing a phase transition between different ferroelectric states [13]. It is also larger than the value of $\simeq 40.6$ pm/V found in tetragonal $BaTiO_3$ [46]. Also note that none of the clamped $r^{\eta}_{ij}$ exhibit any significant change when crossing the boundaries between Regions II, III and IV.

For the case of unclamped EO coefficients, we just show $r^{\sigma}_{13}$ and $r^{\sigma}_{33}$ in Fig. 3(b), because, unlike for $r^{\sigma}_{22}$ and $r^{\sigma}_{42}$, they are found to be significantly enhanced from their clamped values in Region II. For instance, at $\eta_{in} \sim -0.7\%$ (that is, the phase boundary between the Regions I and II) unclamped $r^{\sigma}_{33} \simeq 196.4$ pm/V and $r^{\sigma}_{13} \simeq -46.8$ pm/V – as compared to the clamped ones equal to $r^{\eta}_{33} \simeq 50$ pm/V and $r^{\eta}_{13} \simeq -10$ pm/V at this epitaxial strain. Figures 3(c) and 3(d) show that the $d^{\text{epi}}_{33}$ coefficients and elasto-optic coefficients $p_{13}$ and $p_{33}$ are maximal and really large in magnitude at this boundary, therefore explaining why the EO coefficients are enhanced in the unclamped case with respect to those of the clamped situation for strains close to $-0.7\%$ – as fully consistent with Eq. (3). In particular, $d^{\text{epi}}_{33}$ adopts a value of $\simeq 435$ pC/N at $\eta_{in} \sim -0.7\%$, which is about 16 times the one found in scandium aluminum nitride alloy thin films ($d_{33} \simeq 27.6$ pC/N) [20]. Similarly, a large value of elasto-optic coefficients $p_{33} \simeq 0.34$ is predicted at the boundary between Regions I and II, with this value being larger than the ones found in most trigonal, tetragonal and hexagonal crystals [47]. It is also worthwhile to realize that the piezoelectric stress coefficient $e_{33}$ of Fig. 3(e) adopts a strong peak at this phase boundary between Regions I and II (as a result of the softening

of an $A_1$ mode and the $P\bar{6}m2$-to-$P3m1$ transition), and that the elastic compliance coefficient $S_{33}^{\rm epi}$ of Fig. 3(f) has a maximum within Region III which corresponds to the saddle point of the total energy peak in Fig. 1(a). Another interesting feature is that $p_{13}$ has an extremum at the boundary between Regions III and IV. On the other hand, $r_{33}^{\sigma}$ and $r_{13}^{\sigma}$ rather smoothly behave in Regions II, III and IV because of the corresponding continuous behavior of their corresponding clamped values as well as the product between the $p_{ij\alpha\beta}$ elasto-optic constants and $d_{\alpha\beta k}^{\rm epi}$ piezoelectric strain coefficients – in line with Eq. (3).

In summary, based on first-principles calculations, we predict the existence of four different strain-induced regions in $1 \times 1$ AlN/ScN superlattices, that are accompanied by an optimization and/or control of several physical properties as well as by striking fundamental features. In particular, the continuous evolution from the $h$-derived phase of Region I to an intermediate state characterizing Region II is driven by a softening of the lowest $A_1$ mode and a phase transition, which naturally lead to very large piezoelectric, electro-optic and elasto-optic responses as well as the appearance of an electrical polarization. Moreover, Region III possesses the maximal value of the $S_{33}^{\rm epi}$ elastic compliance, and exhibits anticrossing between two phonon modes of identical $A_1$ symmetry on its right border. A subtle Region IV is further identified, mostly based on anomalies in electronic band structure and lowest magnitude of the $p_{13}$ elasto-optic coefficient. It is also remarkable that the strain evolution from $-6\%$ to $+6\%$ (from Regions I to IV, via Regions II and III) allows (i) a systematic control of the magnitude of the polarization from a null to rather large value of $1.07$ C/m$^2$; and (ii) the electronic band gap to cover a large range of the electromagnetic spectra including cyan, blue, violet, near and middle ultraviolet. Interestingly, the Supplemental Material [22] further demonstrates that many of these spectacular effects still hold when investigating epitaxial $1 \times 3$ AlN/ScN superlattices, with the discovery of the largest electro-optic and elasto-optic coefficients ever predicted or measured. We thus hope that this Letter will encourage the experimental investigation of superlattices made from rather dissimilar materials in the search for optimization and control of properties, as well as the observation of unusual features, and the design of multifunctional devices.

This work is supported by the National Natural Science Foundation of China (Grants No. 11804138 and No. 11825403), the Special Funds for Major State Basic Research (Grant No. 2015CB921700), the Qing Nian Ba Jian Program, the Fok Ying Tung Education Foundation, and China Postdoctoral Science Foundation (Grant No. 2018M641905). D.V. acknowledges ONR Grant N00014-16-1-2951. C.P. and L.B. thank the ARO Grant No. W911NF-16-1-0227. L.B.

also acknowledges the DARPA grant HR0011-15-2-0038 (MATRIX program).

* hxiang@fudan.edu.cn

† laurent@uark.edu

[1] R. F. Gibson, Compos. Struct. **92**, 2793 (2010).

[2] A. F. Wright and J. S. Nelson, Phys. Rev. B **51**, 7866 (1995).

[3] C. Bungaro, K. Rapcewicz, and J. Bernholc, Phys. Rev. B **61**, 6720 (2000).

[4] N. Farrer and L. Bellaiche, Phys. Rev. B **66**, 201203(R) (2002).

[5] V. Ranjan, L. Bellaiche, and E. J. Walter, Phys. Rev. Lett. **90**, 257602 (2003).

[6] C. Constantin, H. Al-Brithen, M. B. Haider, D. Ingram, and A. R. Smith, Phys. Rev. B **70**, 193309 (2004).

[7] E. Bousquet, M. Dawber, N. Stucki, C. Lichtensteiger, P. Hermet, S. Gariglio, J.-M. Triscone, and Ph. Ghosez, Nature (London) **452**, 732 (2008).

[8] N. A. Pertsev, A. K. Tagantsev, and N. Setter, Phys. Rev. B **61**, R825 (2000).

[9] J. H. Haeni *et al.*, Nature (London) **430**, 758 (2004).

[10] Z. Jiang , R. Zhang , D. Wang, D. Sichuga, C. L. Jia, and L. Bellaiche, Phys. Rev. B **89**, 214113 (2014).

[11] L. Chen, Y. Yang, Z. Gui, D. Sando, M. Bibes, X. K. Meng, and L. Bellaiche, Phys. Rev. Lett. **115**, 267602 (2015).

[12] X.-Z. Lu and J. M. Rondinelli, Nat. Mater. **15**, 951 (2016) .

[13] C. Paillard, S. Prokhorenko, and L. Bellaiche, npj Comput. Mater. **5**, 6 (2019).

[14] V. Ranjan, S. Bin-Omran, L. Bellaiche, and A. Alsaad, Phys. Rev. B **71**, 195302 (2005).

[15] W. I. F. David, P. P. Edwards, M. R. Harrison, R. Jones, and C. C. Wilson, Nature (London) **331**, 245 (1988).

[16] L. Bellaiche, K. Kunc, and J. M. Besson, Phys. Rev. B **54**, 8945 (1996).

[17] A. L. J. Pereira, J. A. Sans, R. Vilaplana, O. Gomis, F. J. Manjón, P. Rodríguez-Hernández, A. Muñoz, C. Popescu, and A. Beltrán, J. Phys. Chem. C **118**, 23189 (2014).

[18] V. Ranjan, S. Bin-Omran, D. Sichuga, R. S. Nichols, L. Bellaiche, and A. Alsaad, Phys. Rev. B **72**, 085315 (2005).

[19] A. Alsaad and A. Ahmad, Eur. Phys. J. B **65**, 65 (2008).

[20] M. Akiyama, T. Kamohara, K. Kano, A. Teshigahara, Y. Takeuchi, and N. Kawahara, Adv. Mater. **21**, 593 (2009).

[21] S. Fichtner, N. Wolff, F. Lofink, L. Kienle, and B. Wagner, J. Appl. Phys. **125**, 114103 (2019).

[22] See Supplemental Material at http://link.aps.org/supplemental/... for more details about (i) computational details; (ii) properties of AlN bulk in its wurtzite structure and ScN bulks in their layered hexagonal and rocksalt structures; (iii) some properties of $1 \times 1$ AlN/ScN superlattices; and (iv) some quantities of $1 \times 3$ AlN/ScN superlattices, which includes Refs. [14, 18, 23–32, 46].

[23] X. Gonze, J.-M. Beuken, R. Caracas, F. Detraux, M. Fuchs, G.-M. Rignanese, L. Sindic, M. Verstraete, G. Zerah, F. Jollet, M. Torrent, A. Roy, M. Mikami, Ph. Ghosez, J.-Y. Raty, and D. C. Allan, Comput. Mater. Sci. **25**, 478 (2002).

[24] D. R. Hamann, Phys. Rev. B **88**, 085117 (2013).

[25] M. Veithen, X. Gonze, and Ph. Ghosez, Phys. Rev. Lett. **93**, 187401 (2004).

[26] M. Veithen, X. Gonze, and Ph. Ghosez, Phys. Rev. B **71**, 125107 (2005).

[27] M. Feneberg, R. A. R. Leute, B. Neuschl, K. Thonke, and M. Bickermann, Phys. Rev. B **82**, 075208 (2010).

[28] H. A. Al-Brithen, A. R. Smith, and D. Gall, Phys. Rev. B **70**, 045303 (2004).

[29] R. Resta, Rev. Mod. Phys. **66**, 899 (1994).

[30] X. Gonze and C. Lee, Phys. Rev. B **55**, 10355 (1997).

[31] D. R. Hamann, X. Wu, K. M. Rabe, and D. Vanderbilt, Phys. Rev. B **71**, 035117 (2005).

[32] X. Wu, D. Vanderbilt, and D. R. Hamann, Phys. Rev. B **72**, 035105 (2005).

[33] H. T. Stokes and D. M. Hatch, J. Appl. Cryst. **38**, 237 (2005).

[34] M. A. Haase, J. Qiu, J. M. Depuydt, and H. Cheng, Appl. Phys. Lett. **59**, 1272 (1991).

[35] F. A. Ponce and D. P. Bour, Nature (London) **386**, 351 (1997).

[36] C. Skierbiszewski, Appl. Phys. Lett. **86**, 011114 (2005).

[37] F. Masuoka, K. Ooba, H. Sasaki, H. Endo, S. Chiba, K. Maeda, H. Yoneyama, I. Niikura, and Y. Kashiwaba, Phys Status Solidi C **3**, 1238 (2006).

[38] R. Phillips, *Sources and Applications of Ultraviolet Radiation* (Academic Press, New York, 1983).

[39] L. Liu and J. H. Edgar, Mater. Sci. Eng. R **37**, 61 (2002).

[40] P.-E. Janolin, A. S. Anokhin, Z. Gui, V. M. Mukhortov, Y. I. Golovko, N. Guiblin, S. Ravy, M. E. Marssi, Y. I. Yuzyuk, L. Bellaiche, and B. Dkhil, J. Phys.: Condens. Matter **26**, 292201 (2014).

[41] R. J. Zeches *et al.*, Science **326**, 977 (2009).

[42] Y. Cao, Q. Li, M. Huijben, R. K. Vasudevan, S. V. Kalinin, and P. Maksymovych, Phys. Rev. Materials **2**, 094401 (2018).

[43] H. Béa *et al*., Phys. Rev. Lett. **102**, 217603 (2009).

[44] E. H. Turner, Appl. Phys. Lett. **8**, 303 (1966).

[45] I. P. Kaminow and W. D. Johnston, Jr., Phys. Rev. **160**, 519 (1967).

[46] M. Zgonik, P. Bernasconi, M. Duelli, R. Schlesser, P. Günter, M. H. Garrett, D. Rytz, Y. Zhu, and X. Wu, Phys. Rev. B **50**, 5941 (1994).

[47] M. J. Weber, *Handbook of Optical Materials* (CRC Press, Boca Raton, FL, 2002).

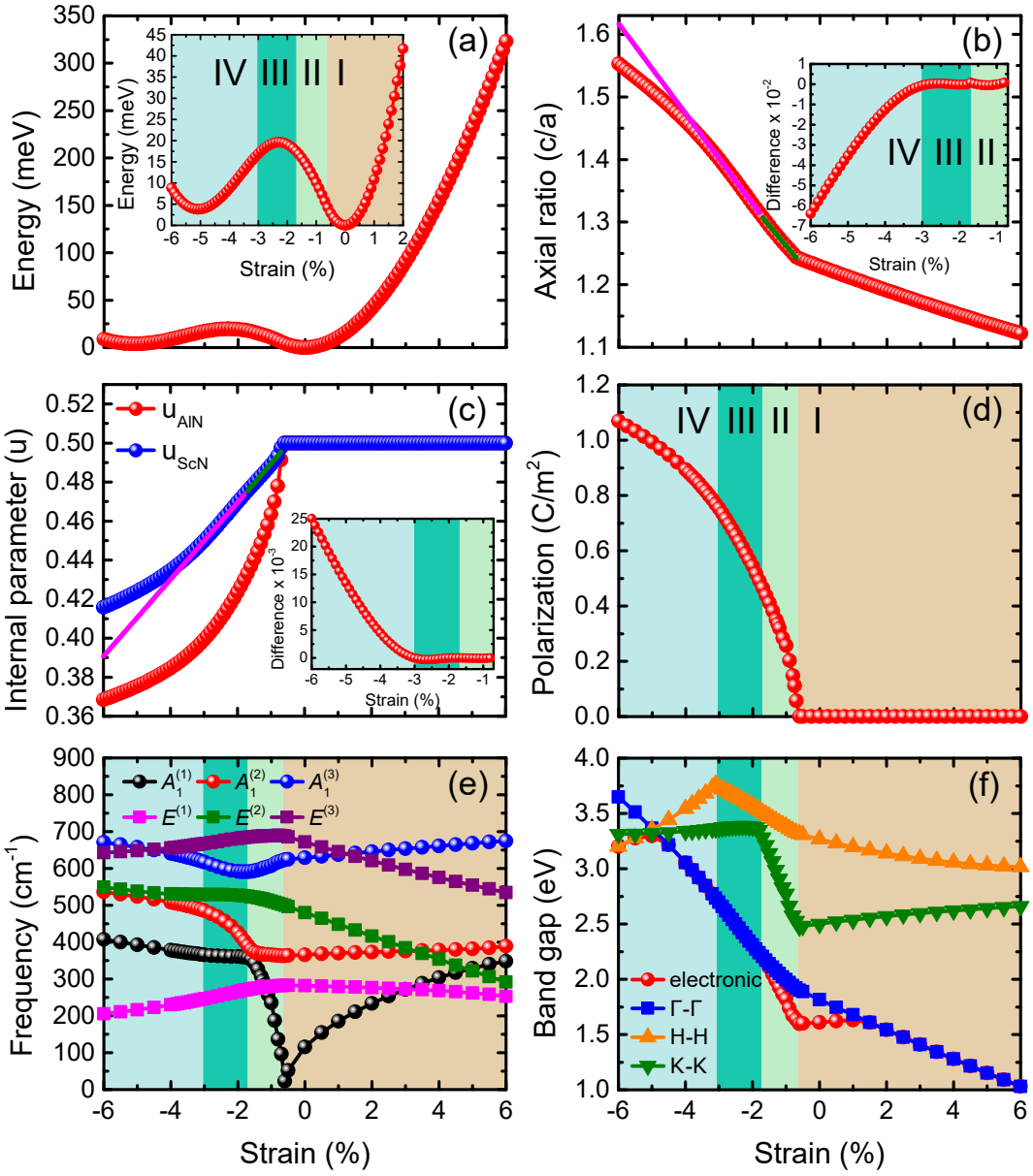


FIG. 1. Structural properties of $1 \times 1$ AlN/ScN as a function of strain: (a) total energy (the inset zooms in the data for strains between $-6\%$ and $+2\%$); (b) axial ratio $c/a$ (the inset shows the difference between the $c/a$ data and two straight lines that pass through Regions II (green line) and III (blue line); (c) internal parameters (the inset shows the difference between the $u_{\mathrm{ScN}}$ data and two straight lines that pass through Regions II (green line) and III (magenta line); (d) polarization $P_z$; (e) phonon spectrum at the $\Gamma$ point of the first Brillouin zone; (f) the electronic band gap and the direct band gaps at $\Gamma$, H and K.

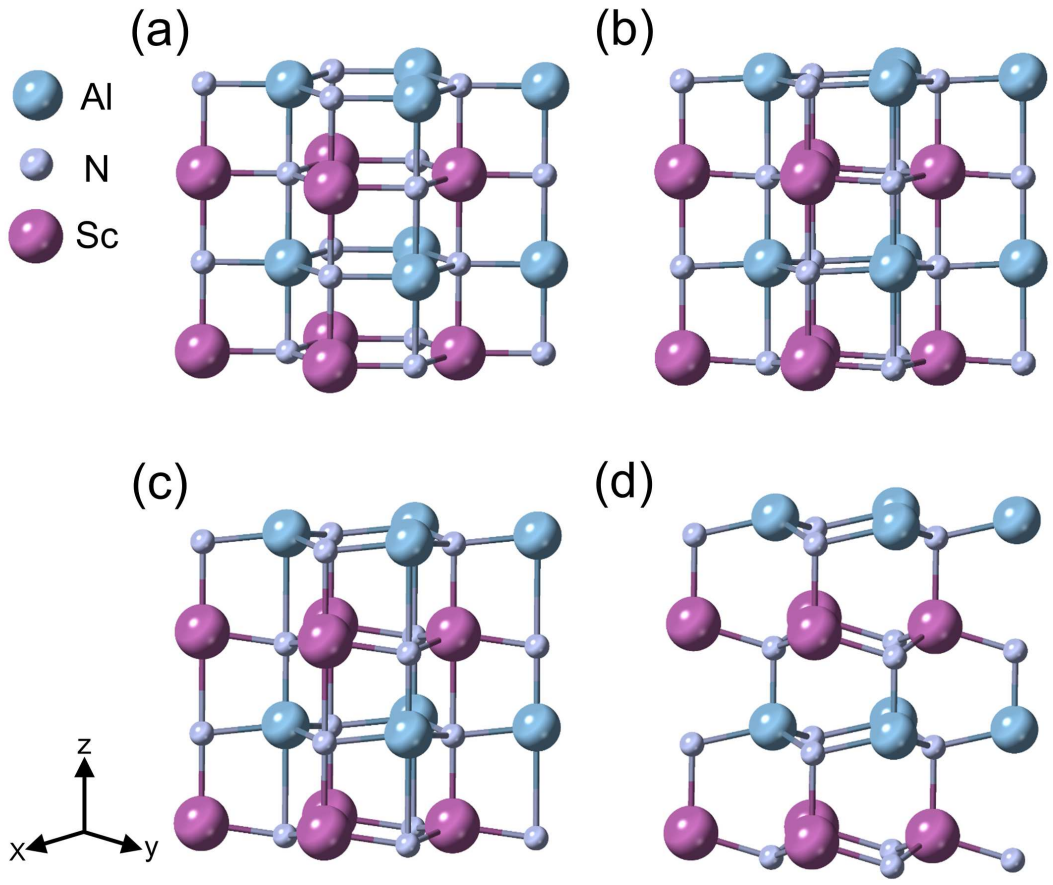


FIG. 2. Crystal structures of the studied $1 \times 1$ AlN/ScN superlattices. Panel (a) depicts the hexagonal-derived structure (for the strain of $0\%$) of Region I. Panel (b) shows an intermediate phase for $\eta_{in} = -1\%$ in Region II. Panel (c) displays an intermediate phase of Region III for $\eta_{in} = -2\%$. Panel (d) shows the wurtzite-derived structure of Region IV in the case of a an epitaxial strain being equal to $-5\%$.

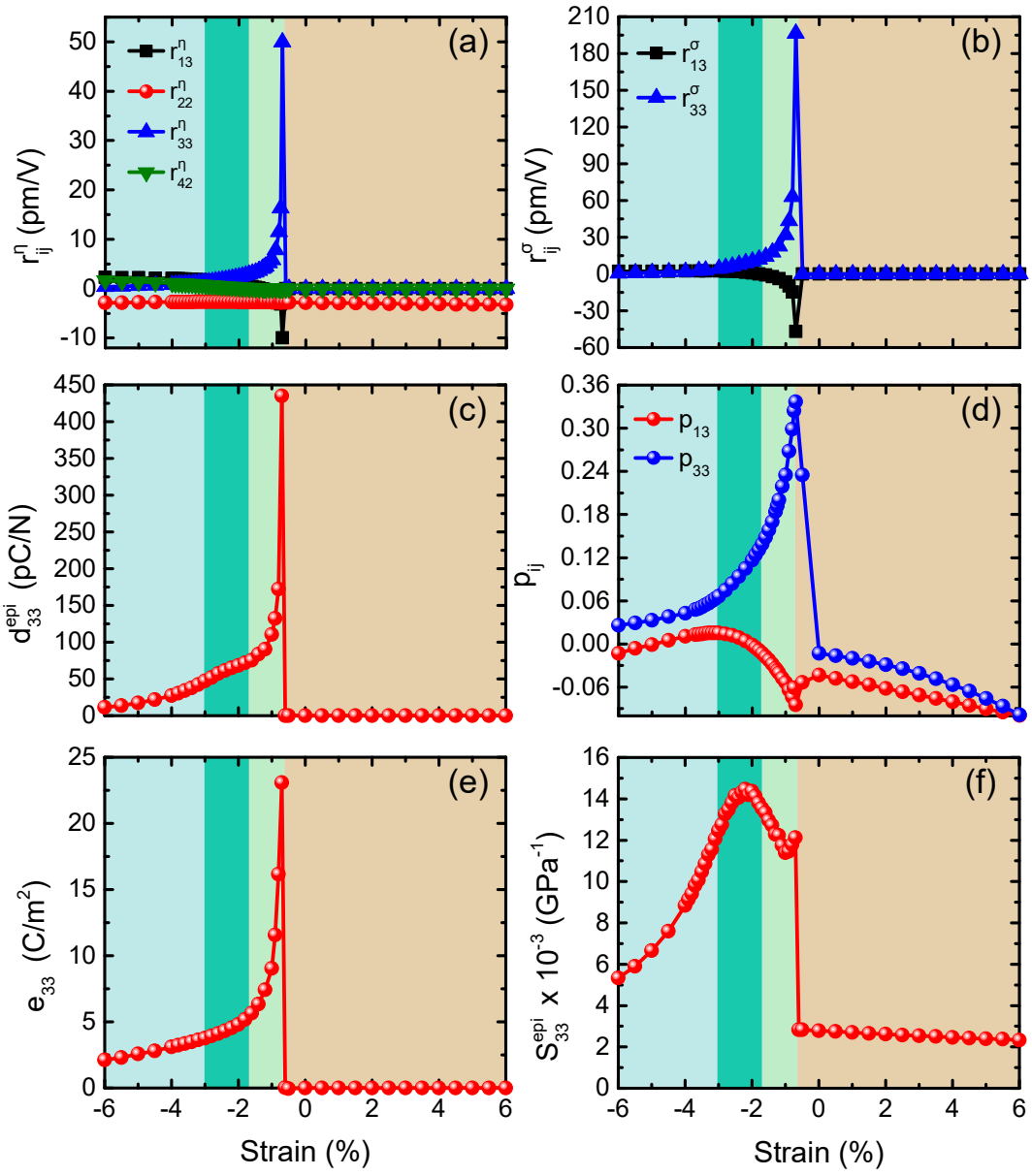


FIG. 3. Evolution with strain of the (a) clamped EO coefficients; (b) unclamped EO coefficients; (c) piezoelectric strain coefficients $d_{33}^{\mathrm{epi}}$; (d) elasto-optic coefficients $p_{13}$ and $p_{33}$; (e) piezoelectric stress coefficients $e_{33}$; and (f) elastic compliance constants $S_{33}^{\mathrm{epi}}$ in the studied $1 \times 1$ AlN/ScN superlattices.